Effect of crystallographic orientations on the hydrogen-induced cracking resistance improvement of API 5L X70 pipeline steel under various thermomechanical processing

Mohammad Masoumi *, Cleiton Carvalho Silva, Hamilton Ferreira Gomes de Abreu

Federal University of Ceará, Department of Metallurgical and Materials Engineering, Campus do Pici, Bloco 729 CEP 60.440-554, Fortaleza, Ceará, Brazil

ARTICLE INFO

ABSTRACT

In this study a thermomechanical processing was suggested to improve the hydrogen-induced cracking (HIC) resistance in X70 pipeline steel. Proposed thermomechanical treatment produced favorable crystallographic textures and significantly increased HIC resistance which is of great interest to petroleum industry. The results showed that the high angle grain boundaries and Kernel parameter values acted as hydrogen-trapping sites, leading to increased HIC susceptibility. Highest HIC resistance was obtained in sample rolled isothermally at 850 °C, due to the high proportion of grains oriented with {110} planes parallel to the normal direction and {111}//ND fibers accompanied by negligible fraction of grains oriented in {001}//ND.

1. Introduction

The continuously increasing demand for crude oil and gas requires the steelmaking industry to improve the corrosion resistance in harsh and aggressive environments. Low carbon steels for sour service piping are widely used for transportation of natural gas and crude oil across long distances because of the low alloying elements content, economic manufacturing and easy installation [1–3]. Stress corrosion cracking (SCC) and hydrogen-induced cracking (HIC), are considered as the main damage modes in the sour environment [4–6] and cause a considerable amount of economic loss to the petroleum industry. Therefore, many strategies have been proposed to reduce HIC susceptibility including adding micro-alloying elements such as titanium, niobium and vanadium, decreasing sulphur and phosphorus contents, controlling the morphology of manganese sulphides, removing precipitation and segregation zones during solution heat treatment and reducing the number of hydrogen trapping [7–9]. However, these strategies have not effectively succeeded to control HIC susceptibility. Therefore, crystallographic texture and grain boundary distributions engineering seems to be a logical step for enhancement of HIC resistance.

Grains oriented in preferred crystallographic orientation that develop during manufacturing process can influence both the mechanical properties and the HIC resistance. The texture of a rolled sheet is represented by a combination of crystallographic plane and direction {hkl}<uvw>, which means that {hkl} are the planes parallel to the rolling plane and the <uvw> are the directions parallel to the rolling direction which is shown in Fig. 1 [10]. Venegas et al. [11,12] studied influence of texture on HIC susceptibility in API X46 steel. They showed that the preferred grain oriented with plane {111} parallel to normal direction ({111}//ND) produced via warm rolling bellow recrystallisation temperature increased the HIC resistance. Ghosh et al. [13] reported that the cleavage {001}//ND grains generated during rolling at high temperature by rescrystallisation of austenite grains followed by ferrite transformation, provide an easy crack path and reduce significantly both the mechanical properties and the HIC resistance. Verdeja et al. [14] documented that the crystallographic textures associated with {110}//ND and {332}//ND reduce the sensitivity to HIC in ferritic-pearlitic steels, while {001}//ND and {112}//ND textures have the opposite effect. Recently, Mohtadi-Bonab et al. [15–17] reported that there is no preferred direction for hydrogen crack propagation, and that crack can propagate along various orientations. However, different factors such as grain orientation, grain boundary distributions, special coincidence site lattice (CSL) boundaries, and distribution of recrystallised grains play significant roles in HIC resistance by providing good lattice fit with low stored energy ahead of the crack tip [18,19]. It is worth mentioning that the

* Corresponding author.
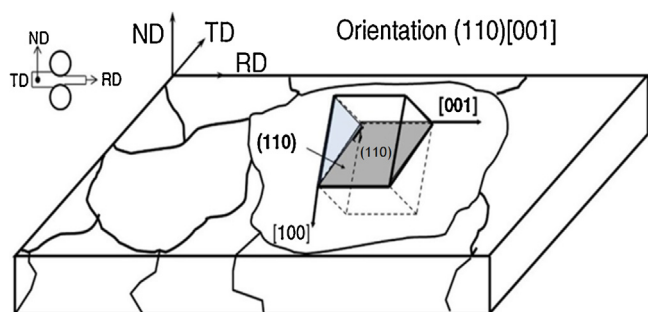E-mail address: mohammad@alu.ufc.br (M. Masoumi).

Fig. 1. Schematic representation of crystal orientation with respect to sample axes [10].

crystallographic texture interpretation is not straightforward and a fundamental understanding of corrosion is required.

In the present work, firstly microstructure and microtexture in the vicinity of hydrogen induced cracks, in a plate taken from an in-service sour gas pipeline were examined to find a correlation between crack propagation and crystallographic textures. Then, a similar material with comparable chemical composition was cut and subjected to thermomechanical processing with various finish rolling temperatures to produce a similar microstructure with different crystallographic textures. Then, to study the effects of different thermomechanical processing on microstructure, macrotexture and microtexture were investigated by scanning electron microscopy (SEM), X-ray energy dispersive spectroscopy (EDS), electron backscatter diffraction (EBSD), and X-ray diffraction (XRD). Finally, electrochemical hydrogen charging tests were carried out to show the HIC resistance improvement via appropriate thermomechanical processing.

2. Experimental procedure

An API 5L X70 plate was taken from an in-service pipeline which was used for about 20 years for sour gas transportation and contained several hydrogen induced cracks. The chemical composition of this sample was 0.105C, 1.664 Mn, 0.018 P, 0.006 S and 0.204 Si (wt.%). In addition, another similar plate with comparable chemical composition (0.099C, 1.604 Mn, 0.014 P, 0.011 S and 0.180 Si (wt.%)) was cut from a 9 mm plate and then subjected to four different thermomechanical processing routes, as shown in Fig. 2.

In order to dissolve inclusions and eliminate probable segregation zones, the samples were solution annealed at 1200 °C for one hour. Then, the samples were rolled in a Stanat model TA-315 rolling machine with 273 rpm rotational speed, in three passes to reach the 3 mm thickness (9 mm → 7 mm → 5 mm → 3 mm), followed by air cooling to room temperature. Temperature tracking during the rolling operation was carried out by Minolta/Land Cyclops 152 Infrared Thermometer. It is worth mentioning that the main idea for the different start and finish rolling temperatures, lower than the recrystallisation temperature (in both austenite and austenite-ferrite regions), was to obtain a similar microstructure with different crystallographic textures.

Microstructural studies were carried out along the cross section (RD-ND) on all samples. The rolled samples were prepared for metallographic analysis by grinding with SiC papers up to 1200 grit and then polishing with 6, 3 and 1 μm diamond paste. Finally, the specimens were etched with 2% nital solution for approximately 40 s and examined using SEM. Also, the micro-hardness test was performed based on the ASTM E-384 standard along the mid-thickness of specimens with 4.903 N indentation load for 15 s (HV0.5).

Macrotextures were measured in mid-thickness along the RD-TD sections (rolling plane). These studies were performed using Panalytical X'Pert Pro diffractometer equipped with Cu radiation

source and texture goniometer. Three incomplete pole figures, i.e. {110}, {200} and {211} were obtained in the reflection mode on a 5° grid up to 85° sample tilt. The orientation distribution function (ODF) of samples was calculated from the measured pole figures using MTEX-free and open source software toolbox. The $\phi_2 = 45°$ section of Euler space was used to display the computed ODFs. Moreover, electron backscattered diffraction (EBSD) analysis was conducted in the RD-ND plane of investigated samples using FEI Quanta FEG 450 scanning electron microscope operating at an acceleration voltage of 20 kV, sample tilt angle of 70°, working distance of 12 mm and 0.5 μm step size. The Channel 5 software and MTEX were used to analyse and display the data.

In order to estimate the HIC resistance, two specimens of each sheet were prepared from the mid-thickness region, considered as the most susceptible area to HIC, and were subjected to the electrochemical hydrogen charging test. The samples were ground up to 1200 grit paper, and then polished with 6, 3 and 1 μm diamond paste to eliminate flux-limiting surface impedances [20]. 0.2 M sulphuric acid solution was used for hydrogen charging, in the electrochemical hydrogen-charging test. Moreover, to prevent the formation of hydrogen bubbles on the surface of the specimen and to increase the amount of hydrogen entering the steel, 3 g/l arsenic trioxide (As_2O_3) was added to the solution. Each sample was then electrochemically charged for 6 h with a constant current of 20 mA/cm^2.

3. Results and discussion

3.1. Microstructure of HIC sample

The in-service sour material with several hydrogen-induced cracks presented a pearlite/ferrite banded microstructure. The typical stepwise hydrogen crack propagation is shown in Fig. 3a and b and is oriented parallel to the rolling direction, besides some deflection towards the normal direction. There was no segregation zone found in the sample by SEM and EDS analysis. However, different types of inclusions were found in the vicinity of the cracks. Some complex carbonitride precipitates such as (Ti, Nb, V)(C, N) were identified by EDS. As shown in Fig. 3, the ferrite/pearlite phase boundaries also enhanced the crack spread. Micro-hardness measurements in two different regions (with and without cracks), demonstrated the significant hardness variation. The hardness was measured as about 200 ± 5 HV in the non-cracked region, while 235 ± 7 HV was measured around the cracked area, which indicated a correlation between hardness and HIC susceptibility.

3.2. Microtexture analysis of HIC sample

Fig. 4 shows the normal direction inverse pole figure (IPF) maps of the HIC cracked sample. The medium angle grain boundaries (MAGBs) with a misorientation between 5 and 15° and high angle grain boundaries (HAGBs) with misorientation greater than 15° are marked as thin and thick black lines, respectively. As shown in the IPF maps, the HIC crack propagated along the boundaries related to the grains oriented with {001}//ND and {111}//ND fibers, which are indicated with red and blue colours, respectively. Since the high angle grain boundaries have higher internal energy in comparison to both low and medium angle grain boundaries, they were considered as the main hydrogen trapping sites, providing easier paths for crack propagation.

Fig. 4a also demonstrates that the hydrogen induced crack propagated along very small grains (i.e. less than 2 μm in diameter). It is expected that very fine grains with large fraction of high angle grain boundaries with high stored energy, increased the number of nascent hydrogen trappings. Then, trapped
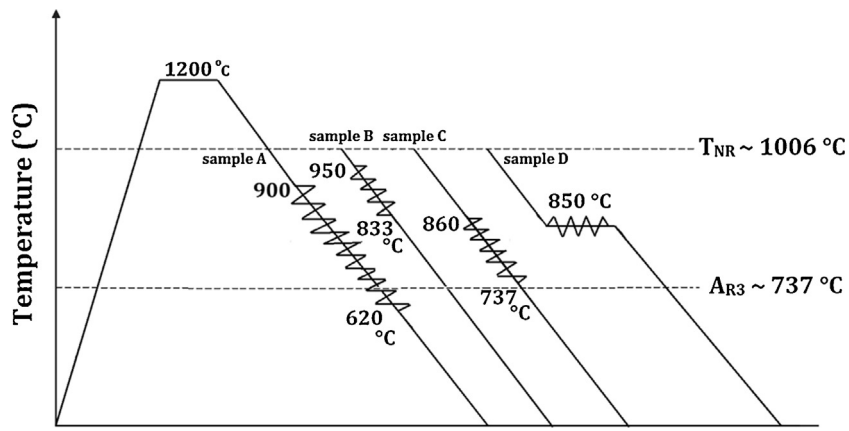
Fig. 2. Schematic representation of thermomechanical processing of samples A–D.
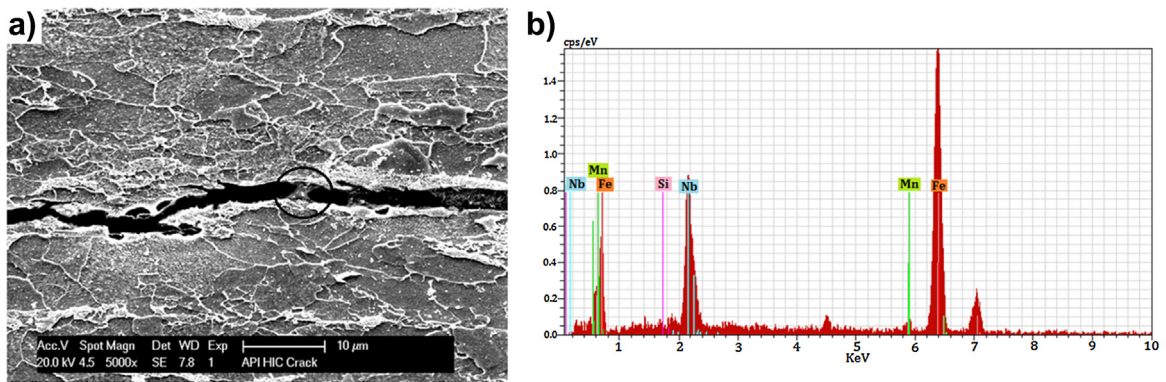

Fig. 3. (a) SEM micrograph, (b) EDS result of the particle in hydrogen crack path.
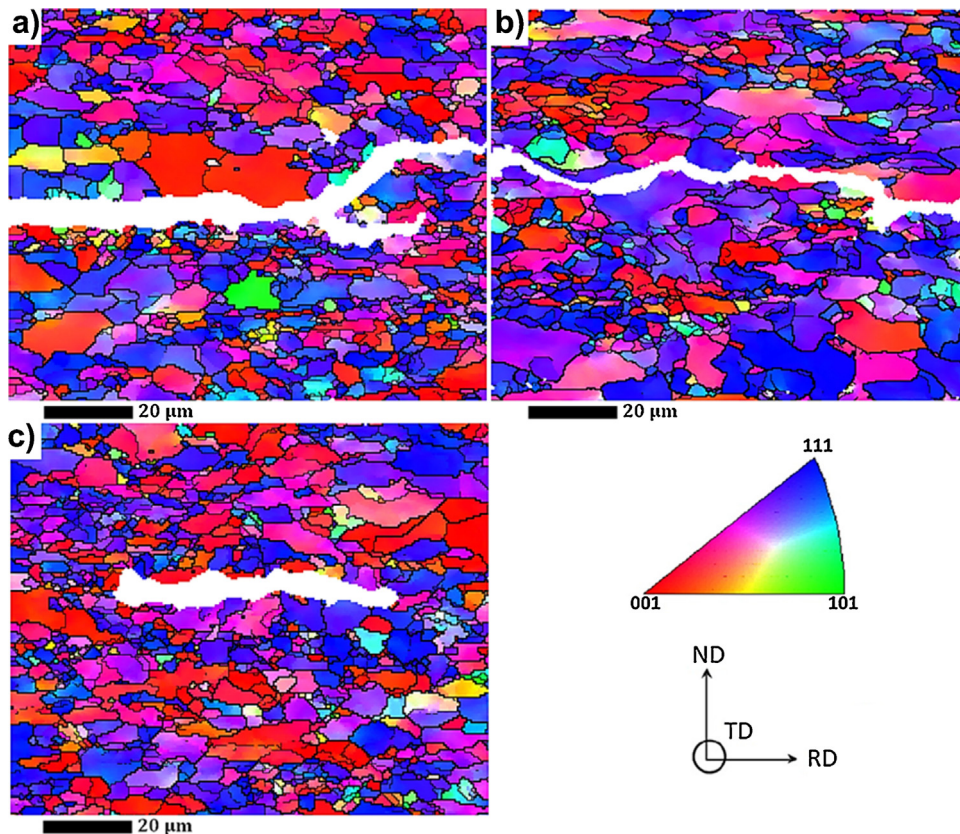

Fig. 4. Inverse pole figure orientation maps in three different regions around hydrogen induced cracks.

hydrogen atoms recombine to form hydrogen molecules, leading to greater internal pressure in material, thus promoting crack nucleation and propagation [21]. In addition, hardness plays a significant role in HIC susceptibility. On the one hand, according the Hall-Petch relation [22,23], the yield strength and hardness increase with decreasing grain size, leading to increased HIC susceptibility. On the other hand, it is believed that the grain boundaries act as obstacles to crack propagation. In the same sample also few very coarse grains (around 18 μm in diameter) were observed in the vicinity of the cracks (Fig. 4a and b). These coarse grains with low fraction of grain boundaries can facilitate crack propagation and increase HIC susceptibility. Therefore, there is an optimum grain size at which maximum HIC resistance can be achieved.

Although the IPF orientation map is an excellent method to present grain orientation, it has an unavoidable limitation in the Euler scheme [24]. To correct this limitation and find a correlation between crack propagation and grain orientations, orientation distribution function was calculated and shown in Fig. 5. The cube texture component with $(001)[0\bar{1}0]$ crystallographic orientation was the dominant texture in the HIC cracked sample (regions A and B). The cube component that developed under shear deformation during thermomechanical processing has a low ability to release the stress or strain concentration. In Fig. 5a and b, the low resistance cleavage path with orientation within 15° of the ideal cube component is considered as the main crack propagation path. In addition, high dislocation density was generated during thermomechanical processing distributed along different slip systems and provided maximum shear stress ahead of crack tip [25,26]. Thus, the zigzag-like crack propagation observed in this sample is related to the above mentioned phenomenon. Also, the $(112)[3\bar{1}\bar{1}]$ component is observed in region C in the vicinity of the crack. The (112) plane is considered as one of the main slip planes in the BCC lattice [27]. As mentioned earlier, dislocation is arranged along this slip plane and provides sufficient driving force for crack propagation.

Another parameter to be evaluated is the Kernel average misorientation (KAM) which represents the relative average misorientation between any points that belong to the same grain [28]. KAM distribution maps for the HIC cracked sample are shown in Fig. 6. According to Ref. [29], hydrogen segregation is localised near the grain boundaries, considered as dislocation accumulation sites. A high accumulation of grains with relative misorientation between 0.5–2.5° is observed. This accumulation suggests that strain induced during both manufacturing process and service develops easier sites and paths to crack formation. Also, the regions near the hydrogen induced cracks showed lower Kernel parameter values due to release of energy near to the crack tip which provides sufficient driving force for crack growth. The results revealed that the crack tended to propagate along grains with high Kernel parameter values. The high dislocation density around the crack path permits the accumulation of misorientations inside the grains and distortion between neighbouring lattices, leading to an increase in HIC susceptibility.

It is deduced that there are three possibilities for HIC crack propagation. The first is that the crack tends to propagate through the deformed grains with high stored energy where dynamic recrystallisation or recovery did not occur. The second is that the crack propagated along grain oriented with {001}//ND, where the lack of sufficient slip systems has a harmful effect on HIC resistance. Besides, deformed grains oriented with {111}//ND and {112}//ND with high dislocation can also provide easier paths to crack propagation. Finally, very fine grains can trap more hydrogen and generate more internal energy to facilitate crack nucleation and propagation.

3.3. Thermomechanical processing

3.3.1. Microstructural analysis

During thermomechanical processing, the samples were firstly solution treated in a furnace at 1200 °C for one hour, then rolled above and below the recrystallisation temperature (Fig. 2), followed by air cooling. The microstructure of specimens after different thermomechanical processing is shown in Fig. 7. The ferrite microstructure with pearlite, martensite-austenite (M/A) constituents and a small fraction of bainite is observed. Furthermore, rolling at a lower temperature in a mixture of austenite and ferrite region (sample A) led to the formation of finer grain size. The ferrite is responsible for increased hardening and the austenite tending to undergo additional hardening by rising number of available sites for ferrite nucleation. Rolling below the recrystallisation temperature developed the pancake-shaped austenite grains, leading to an increase in the number of nucleation sites for the austenite-to-ferrite transition to form polygonal ferrite.

Hardness measurements were carried out at the mid-thickness of specimens. The hardness increased with decreasing finish rolling temperature. The measured hardness values in samples A, B, C and D were 224, 211, 234 and 220 ± 5HV0.5, respectively. According to the API 5L requirements for equipment in severe wet H_2S service [30], hardness shall be lower than 248 ± 6HV (22HRC). Therefore, all specimens met the hardness requirements of the API 5L specification. Overall, a similar microstructure was obtained in all samples. This is essential here, because the different behaviour of HIC resistance could be only attributed to the differences in crystallographic textures produced via different thermomechanical processing.

3.3.2. Macrotexture

The crystallographic texture and grain boundary distributions in four different thermomechanical processing were studied to find an appropriate texture to attain a higher HIC resistance. Fig. 8 shows the orientation distribution function at $\phi_2 = 45°$ in the RD-TD plane in these specimens. (001)<1$\bar{2}$0> texture components with low HIC resistance were developed in sample A during recrystallisation in austenitic region followed by ferrite transformation. Also, deformation at a lower temperature in a mixture of austenite and ferrite phases caused the strong formation of {111}//ND fiber. However, the shear strain generated by friction between the rolls and surface sheet during rolling, developed grains oriented in {110}//ND directions, which is shown in Fig. 8a. It is worth mentioning that the (11)<1$\bar{2}$1> texture components are a consequence of the recrystallisation of ferrite grains [31]. In addition, the highest texture intensity of the ODFs belongs to sample A, which rolled in the ferrite-austenite region. Raabe et al. [32] showed that dislocation sliding during rolling at elevated temperature (above $T_m/4$) extensively took place in the BCC structure on the {110} and {112} planes, leading to decreasing the intensity of crystallographic texture.

The cleavage {001}//ND texture components including $(001)[0\bar{1}0]$, (001)<1$\bar{3}$0>, (001)<1$\bar{2}$0> and (001)<1$\bar{1}$0> were developed in sample B, which was rolled at a higher finish rolling temperature (833 °C), could be attributed to recrystallisation of austenite followed by ferrite transformation. The presence of these textures increases the number of possible crack propagations and HIC susceptibility [8]. Also, the formation of {112}//ND components, that dominate the $(112)[0\bar{2}1]$ and $(112)[\bar{1}11]$ orientations, was observed in this condition. Singh et al. [33] reported that the shear strain during plastic deformation in the austenite phase can develop the $(112)[1\bar{1}0]$ component due to its low stacking fault energy. Then, dynamic recrystallisation and austenite to ferrite phase transformation led to the formation of grains with the $(112)[0\bar{2}1]$ orientation. It is notable that the plastic deformation of the FCC austenite phase occurs by slip or twinning system. Hu [34] reported that the formation of grains with the $(112)[\bar{1}\bar{1}1]$
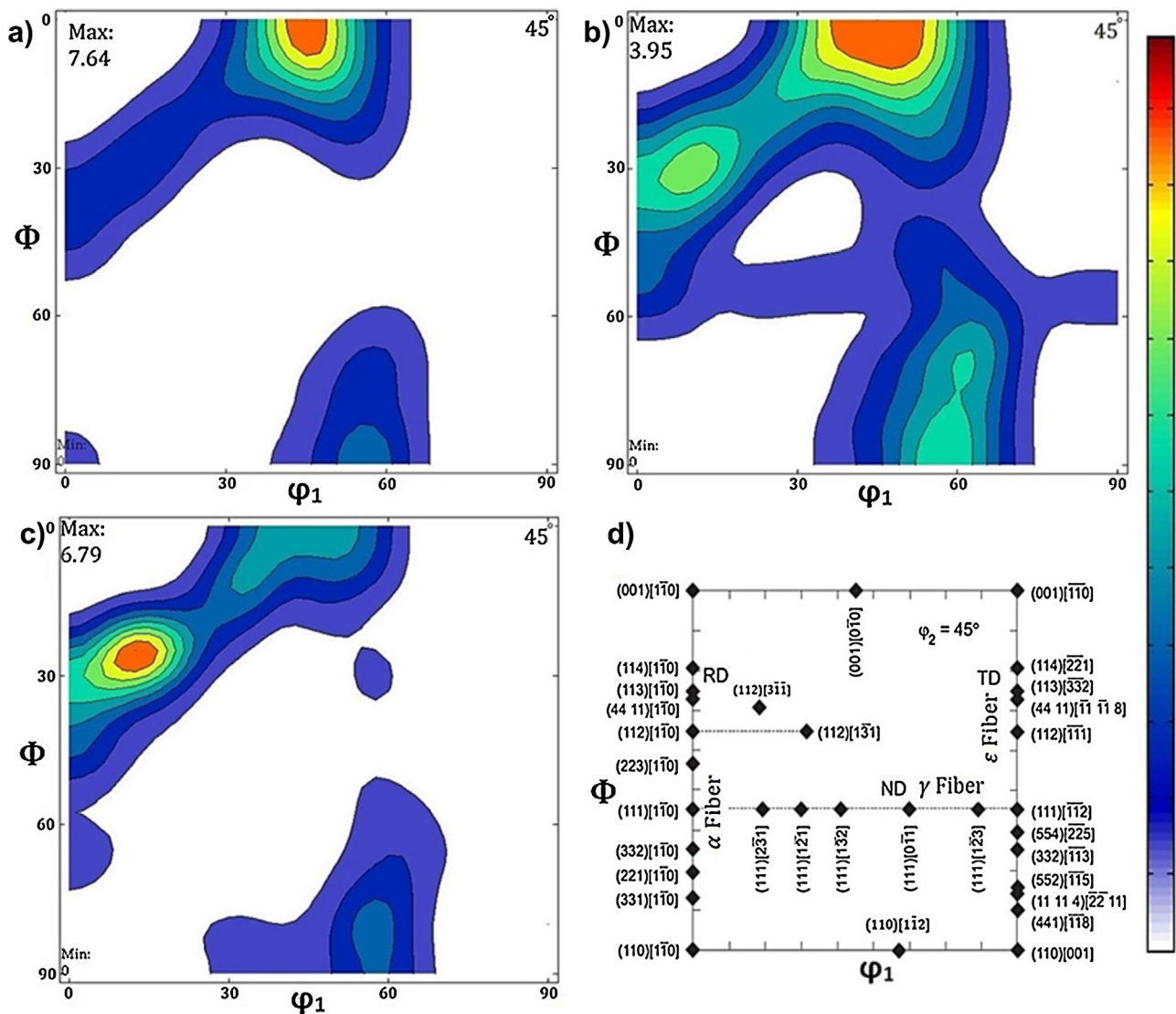
Fig. 5. Calculated texture components at constant $\phi_2 = 45°$ orientation distribution function section from three different regions shown in Fig. 4.

orientation is mostly related to the twinning system, because of low crystal symmetry. Furthermore, the crystallographic texture in sample C was similar to sample B, but the intensity of the {112}//ND fiber decreased at low finish rolling temperature (737 °C). Interestingly, the isothermal rolling at 850 °C (sample D) could hinder the development of undesirable {001}//ND components. The (110)[1$\bar{1}$3] texture component with a spread towards the Goss component with (110)[001] orientation was dominant in sample D.

It was demonstrated that the crystallographic orientation can improve the HIC resistance by well-development of {111}//ND and {110}//ND textures, and reducing the number of cleavage {001}//ND components [8]. Fig. 9 presents the orientation volume fraction (*f(g)*) of fiber components such as {001}, {112}, {111}, and {110}//ND calculated by MTEX software with a 2.5° deflection. For the purpose of textural design, the best resistance against crack propagation results in minimising the {001} cleavage planes that are oriented parallel to the normal direction, and increasing the desirable {110}, {111} and {112}//ND fiber components that are close to the compact planes. The formation of strong covalent bonds between two lattices linked together by close-packed plane leads to obstacles to crack propagation, and increases HIC resistance. As shown in Fig. 9 the first three samples were not suitable for sour

environment, due to the high volume fraction of undesired {001} oriented grains. In contrast, sample D presented sharp {110}//ND and {111}//ND texture components, accompanied by a negligible volume fraction of {001}//ND oriented grains, and considered to be suitable for use in sour environment.

3.3.3. Microtexture

All specimens were examined by the EBSD technique in order to analyse crystallographic orientations, average misorientation angles, grain boundary types and Taylor factor. The inverse pole figure (IPF) maps of samples are shown in Fig. 10. It is worth noting that equiaxed, strain-free recrystallised grains surrounded by high angle grain boundaries as a result of hot-rolling have high resistance to crack nucleation and propagation [35]. Conversely, elongated grains with stored energy are prone to HIC. Moreover, this inhomogeneous microstructure can boost the HIC susceptibility in the final structure. The grain size is another efficient factor to control HIC resistance [36].

The various thermomechanical treatments resulted in a wide distribution range of grain orientations in the specimens. Rolling at a relatively low temperature (i.e. below Ar$_3$) generated a higher dislocation density in samples A and C. Thus, dislocation accumulation inside grains leads to grain subdivision with highly stored
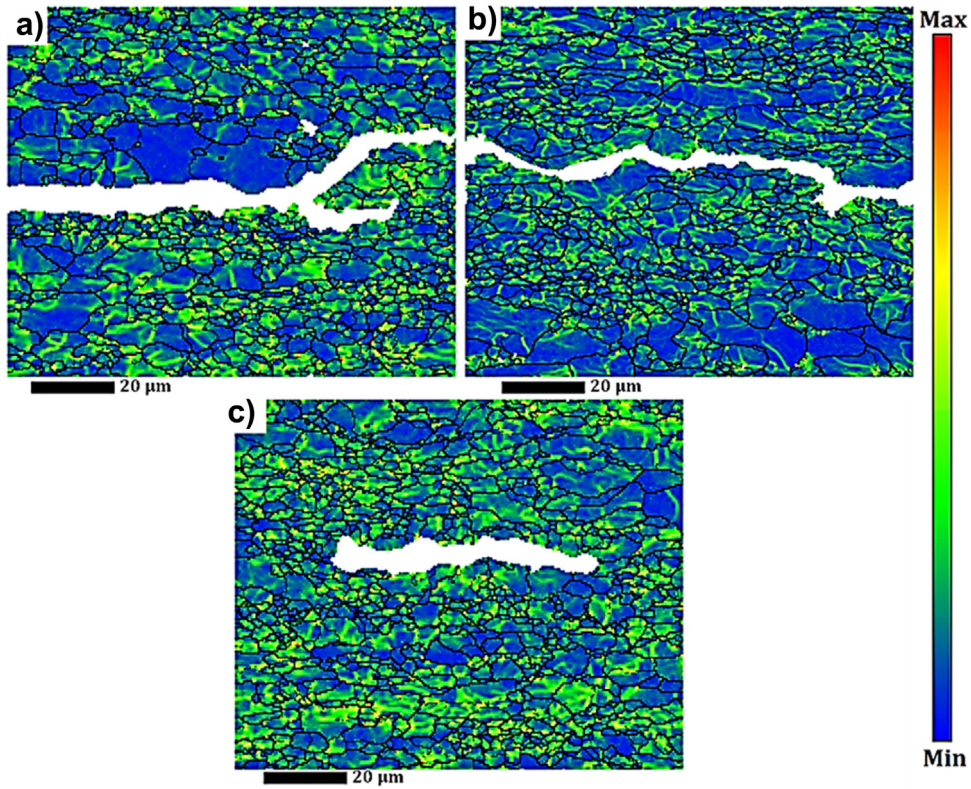
Fig. 6. Kernel average misorientation map in three different regions shown in Fig. 4 from HIC sample.
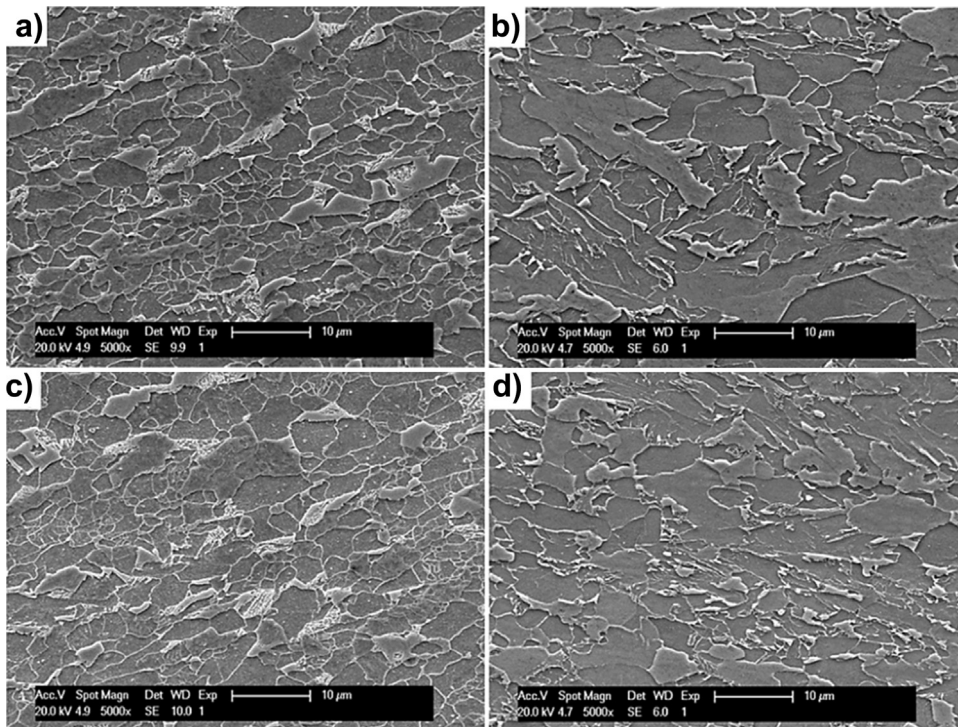

Fig. 7. SEM micrographs showing microstructure of specimens after different thermomechanical processing (a) sample A, (b) sample B, (c) sample C and (d) sample D.

energy which facilitates HIC cracking. Furthermore, for sample B that was rolled at a relatively high temperature (above $T_m/2$), the degree of deformation decreased by recrystallisation in the austenite phase. Dynamic recrystallisation took place in this sample generated the undesirable $(001)[0\bar{1}0]$ cube texture component,

which increases the HIC susceptibility. Also, the IPF map of sample B showed an accumulation of large grains oriented with {001} parallel to the normal direction (red colour). Based on the previous section, {001}//ND dominant grain orientations are highly susceptible to crack initiation and propagation. Finally, the favorable
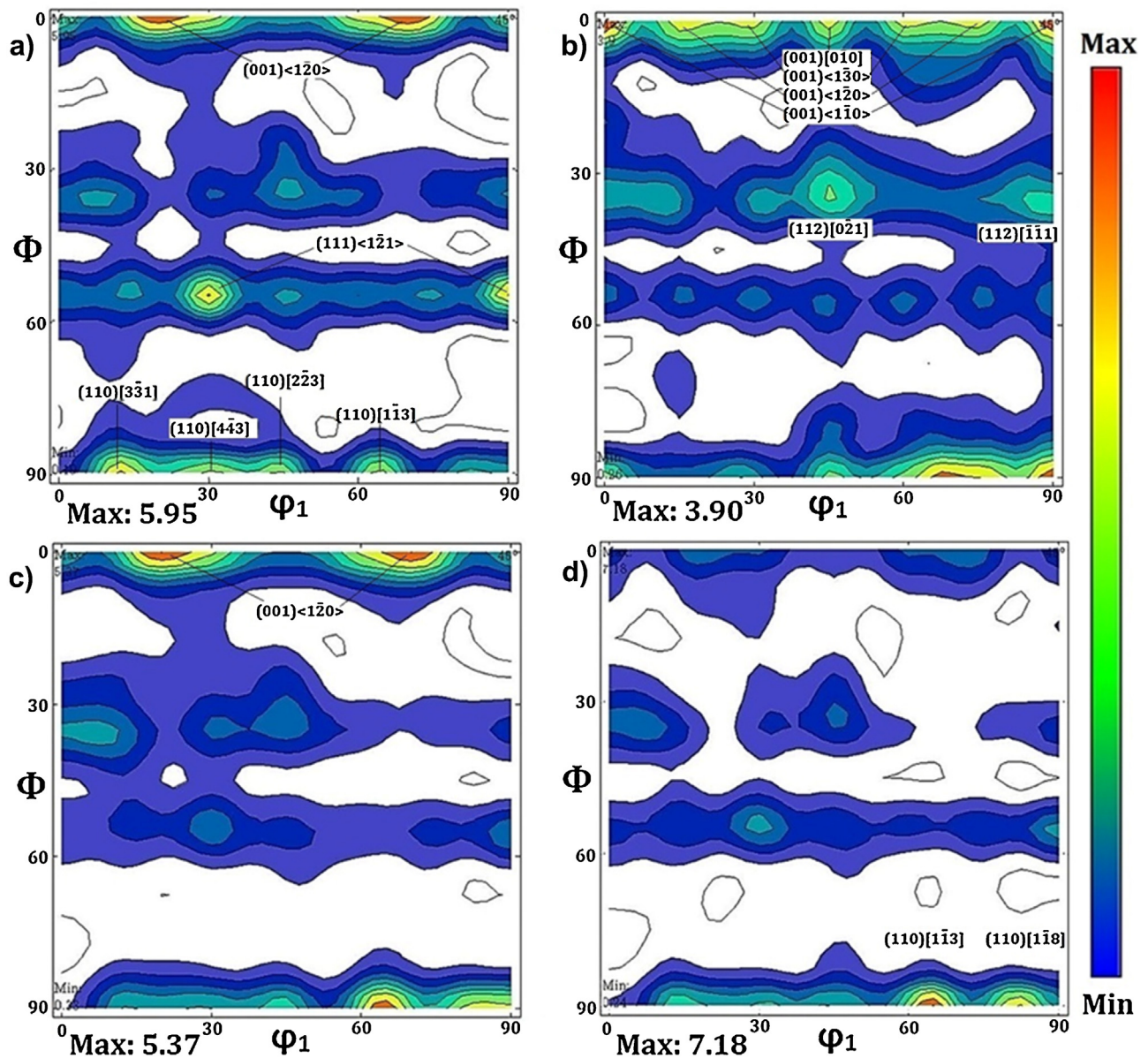
Fig. 8. Texture components at constant $\phi_2 = 45°$ orientation distribution function section in (a) sample A, (b) sample B, (c) sample C and (d) sample D.

$(112)[2\bar{4}1]$ and $(110)[1\bar{1}1]$ texture components were developed by isothermally hot rolling at 850 °C (sample D).

The analysis of EBSD maps led to other interesting microstructural interpretations regarding the differences of grain-boundary angles between adjacent grains. The volume fraction of low, medium and high angle grain boundaries for both HIC cracked and thermomechanically processed specimens was calculated using MTEX software and is shown in Fig. 11. It is clearly observed that the high stored energy as consequence of a large fraction of high angle grain boundaries in HIC cracked sample led to increasing the HIC susceptibility. In other words, HIC resistance depends on the ability of microstructure and precipitates to trap hydrogen. The high angle grain boundaries with high disorder between neighbouring grains and high density of dislocations and vacancies are considered as effective hydrogen trapping sites. It is also believed that high angle boundaries with high lattice distortion and high stored energy provide an easier path to crack nucleation and propagation. Therefore, an increased number of low angle and coincidence site lattice (CSL) boundaries are favorable for improvement of HIC

resistance. Although thermomechanical processing reduced significantly proportion of high angle grain boundaries, there was no significant change observed in CSL boundaries. Therefore, it was confirmed that the HIC susceptibility increases with increased proportion of high angle grain boundaries, and its fraction was found higher in all regions of HIC sample.

As mentioned earlier, plastic deformation at crystal scales is considered by lattice orientation along dislocation arrays, can be observed by Kernel average misorientation. The frequency of Kernel parameter distribution in deferent regions of HIC sample and TMCP specimens is shown in Fig. 12. The high Kernel parameter values belong to HIC sample. It means that the high Kernel parameter values correspond to higher HIC susceptibility. Moreover, the presence of very high Kernel parameter values exceeding 2.5° is observed in HIC sample, facilitate hydrogen crack propagation. Samples B and D have maximum frequencies of low Kernel parameter values (less than 0.5°), which led to high HIC resistance in these samples (Fig. 12). Furthermore, high relative frequencies of low Kernel parameter values (less than 2.5°) were found in sam-
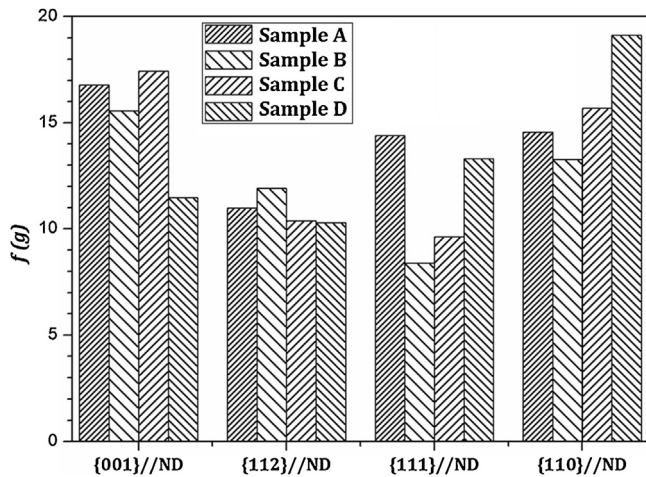
Fig. 9. Volume fractions of fiber components in specimens A–D after different thermomechanical processing.

Fig. 11. Grain boundary distributions in samples A–D in addition to sample with hydrogen induced cracks where LAGBs means low angle grain boundaries, MAGBs means medium angle grain boundaries, HAGBs means high angle grain boundaries and CSL means coincidence site lattice.

ples B and D, where new recrystallised grains with low dislocation density were nucleated. In other words, the recovery and dynamic recrystallisation by annihilation and dislocation rearrangements can significantly reduce the Kernel parameter values and HIC susceptibility. Therefore, an improvement of HIC resistance in the mentioned specimens is expected.

The Taylor factor, which demonstrates a correlation between yield stress and crystal orientation in metals, is used to analyse the level of plastic deformation, showing the distribution of grain orientation [37,38]. Taylor factor analyses were performed on cracked and thermomechanically processed specimens, shown in Fig. 13.
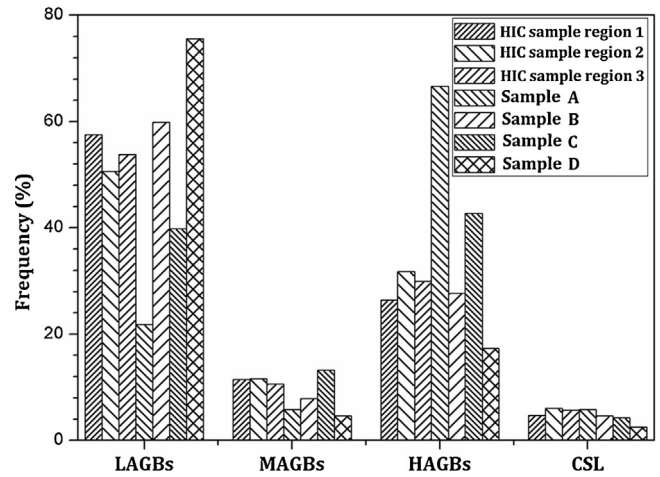
Some grains that are already aligned in the loading direction can easily slip and deform, since the critical resolved shear stress (τ_{crss}) is attained. These grains have a low Taylor factor value. Secondly, the grains that are not already aligned in slip planes regarding stress state. Thus, there needs to be some kind of rotation into a new position to bring out minimum τ_{crss} to slip. These grains with moderate Taylor factor value are called soft grains. Finally, there are some grains that cannot rotate to bring the appropriate slip systems. Therefore, such grains are called hard grains, with a high
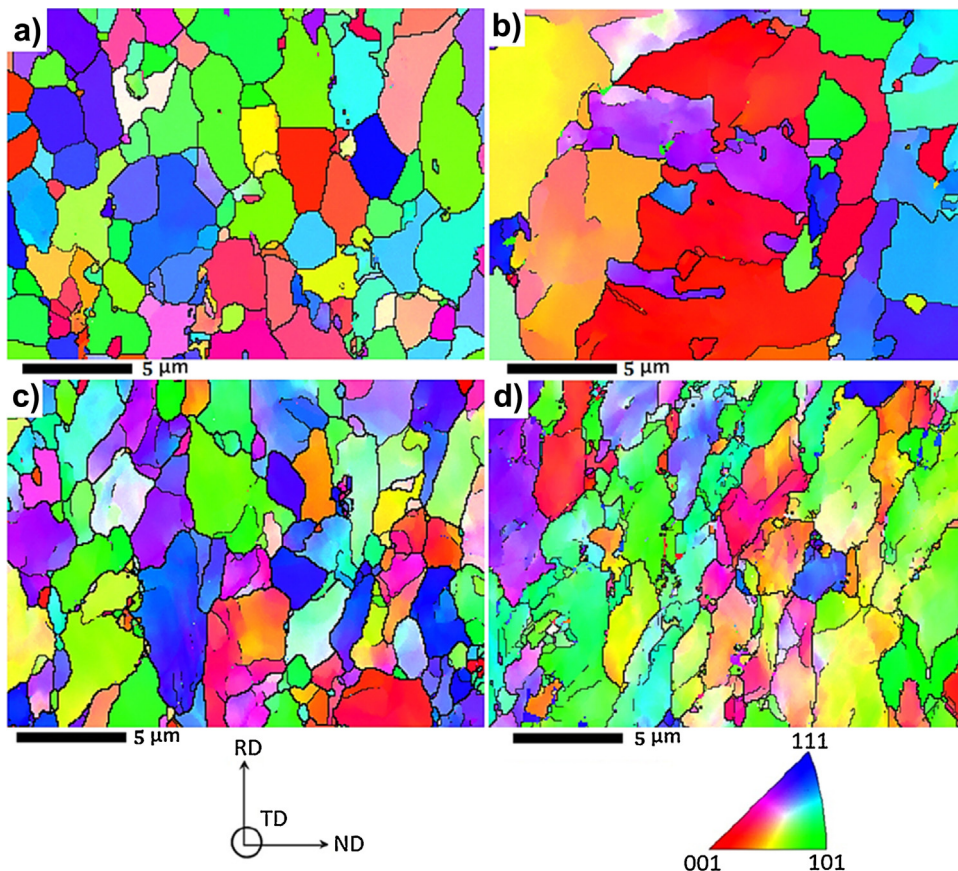

Fig. 10. Inverse pole figure orientation map in (a) sample A, (b) sample B, (c) sample C and (d) sample D.
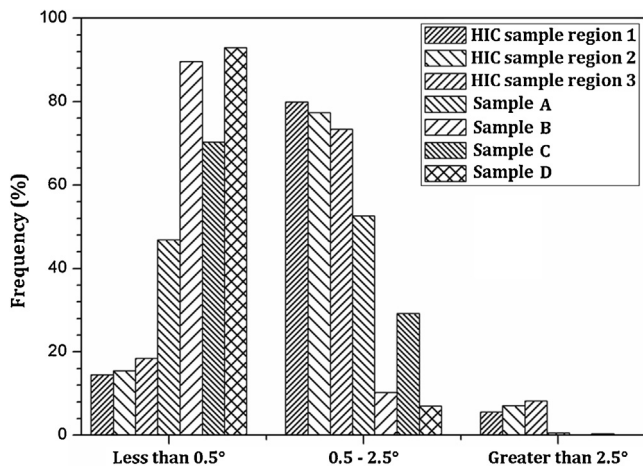
Fig. 12. Frequency distribution of Kernel average misorientation in samples A–D in addition to HIC sample.
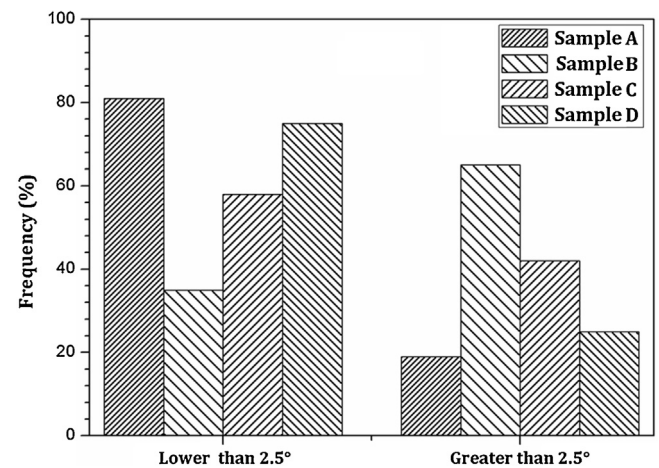
Fig. 14. Taylor factor distribution in samples A–D.

resistance to deformation, and are highly prone to crack formation and propagation, as indicated by the red colour in the Taylor factor maps. Fig. 13 displays the distribution of Taylor factor in the TMCP samples. The grains indicated in light yellow present a relatively easy path and might resist crack propagation; whereas those in dark yellow and red are prone to crack formation. Transgranular crack propagation occurs through the grains with high Taylor factor and dislocation accumulation, while intergranular cracks propagate due to the Taylor factor mismatch in neighbouring grains because of differences in active slip systems. The grain having a high Taylor factor tends to be resistant to yielding, thus transgranular cracking is expected [39]. Intergranular cracks occurred along crack propagation paths between adjacent grains identified by different Taylor factor mismatches.

Active slip systems depend on the crystallographic orientation and the differences of local stress near grain boundaries between adjacent grains [40]. The frequency distribution of Taylor factor values in TMCP samples is presented in Fig. 14. Samples A and D

had low Taylor values. This means that there was less resistance to dislocation movement. On the other hand, samples B and C developed high-stress concentration near the grain boundaries due to the high resistance against dislocation movement, leading to crack formation and providing an easier path for crack propagation. In other words, grain boundary sliding is restricted by their neighbouring grains with high local stress differences, collaborated by crystallographic orientation.

From the mentioned crystallographic texture and grain boundary characteristic investigations, it could be concluded that the sample D had the best HIC resistance. This means that the highest HIC resistance results in sample D, which was rolled isothermally at 850 °C, due to the sharp {110} and {111} texture components accompanied by the negligible volume fraction of grains oriented with {001}//ND. Also, a large amount of low angle grain boundaries with little lattice distortion and low stored energy with the least Taylor factor and Kernel parameter values provided lower trap hydrogen sites. Finally, to ascertain the role of crystallographic texture and grain boundary characteristics, sample C and D were
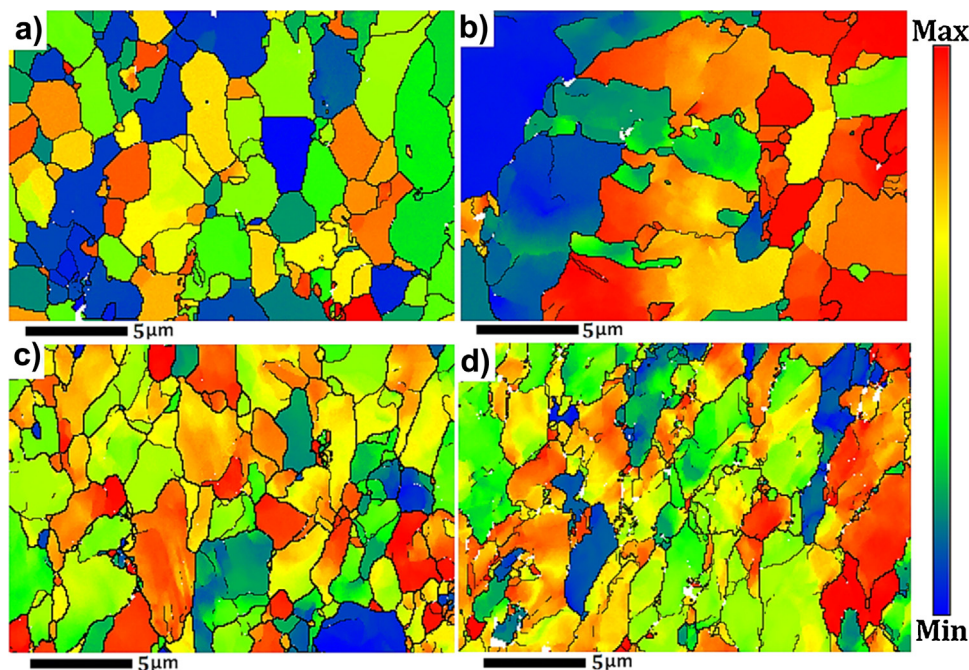

Fig. 13. Taylor factor map in (a) sample A, (b) sample B, (c) sample C and (d) sample D.
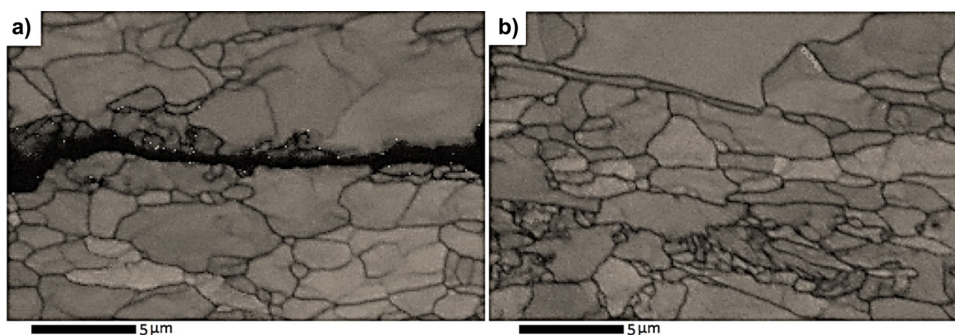
Fig. 15. SEM micrographs of electrochemically charged (a) sample C, (b) sample D.

selected to conduct an electrochemical hydrogen charging experiment. Fig. 15a shows the HIC crack propagation in the sample C after 6 h. The sample D showed high resistance to crack formation, and no HIC cracks were found in the cross section of this sample after hydrogen charging (Fig. 15b). This supports the hypothesis of beneficial effects of crystallographic texture on HIC resistance. Experimental data obtained in this work can be used to enhance accuracy of numerical models [41,42].

4. Conclusions

In this work, several analyses were used to identify the effects of microstructure, precipitations, and crystallographic orientation on HIC susceptibility. Then, the influence of different thermomechanical treatments on microstructure, macro- and microtexture were studied. Finally, an electrochemical hydrogen charging experiment was performed to verify the hypothesis of beneficial effects of crystallographic texture on HIC resistance. The following conclusions can be drawn:

1. HIC cracks propagated not only through {001}//ND oriented grains, but also along the grains oriented with {111}//ND.
2. The high dislocation density around the crack propagation path permits the accumulation of misorientations inside the grains, or distortion between neighbouring lattices, leading to an improvement in HIC susceptibility.
3. Grain boundary distribution played a significant role in HIC susceptibility. High angle grain boundaries and high Kernel parameter values acted as hydrogen-trapping sites, leading to increasing the HIC susceptibility.
4. A poor resistance to HIC was attributed to the presence of strong {001}//ND texture components. Conversely, a reduction in its volume fraction and development of desired texture components improved HIC resistance.
5. The recovery and dynamic recrystallisation by annihilation and dislocation rearrangements can significantly reduce the Kernel parameter values and HIC susceptibility.
6. The highest HIC resistance results in sample D, which was rolled isothermally at 850 °C, due to the sharp {110} and {111} texture components accompanied by the negligible proportion of {001}//ND oriented grains.

Acknowledgements

References

[1] R.A. Carneiro, R.C. Ratnapuli, V.F.C. Lins, The influence of chemical composition and microstructure of API linepipe steels on hydrogen induced cracking and sulfide stress corrosion cracking, Mater. Sci. Eng. A 357 (2003) 104–110.
[2] L.W. Tsay, Y.C. Chen, S.L.I. Chan, Sulfide stress corrosion cracking and fatigue crack growth of welded TMCP API 5L X65 pipe-line steel, Int. J. Fatigue 23 (2001) 103–113.
[3] V.F.C. Lins, M.L.M. Ferreira, P.A. Saliba, Corrosion resistance of API X52 carbon steel in soil environment, JMR & T 1 (2012) 161–166.
[4] Y. Sun, H. Fujii, H. Imai, K. Kondoh, Suppression of hydrogen-induced damage in friction stir welded low carbon steel joints, Corros. Sci. 94 (2015) 88–98.
[5] M. Stipaničev, O. Rosas, R. Basseguy, F. Turcu, Electrochemical and fractographic analysis of Microbiologically Assisted Stress Corrosion Cracking of carbon steel, Corros. Sci. 80 (2014) 60–70.
[6] Z.Y. Liu, X.G. Li, C.W. Du, L. Lu, Y.R. Zhang, Y.F. Cheng, Effect of inclusions on initiation of stress corrosion cracks in X70 pipeline steel in an acidic soil environment, Corros. Sci. 51 (4) (2009) 895–900.
[7] A. Ikeda, T. Kaneko, Y. Ando, On the evaluation method of sulfide stress cracking susceptibility of carbon and low alloy steels, Corros. Sci. 27 (11) (1987) 1099–1115.
[8] K. Matsumoto, Y. Kobayashi, K. Ume, K. Murakami, K. Taira, K. Arikata, Hydrogen induced cracking susceptibility of high-strength line pipe steels, Corros. Sci. 42 (1986) 337–345.
[9] D. Hejazi, A.J. Haq, N. Yazdipour, D.P. Dunne, A. Calka, F. Barbaro, Effect of manganese content and microstructure on the susceptibility of X70 pipeline steel to hydrogen cracking, Mater. Sci. Eng. A 551 (2012) 40–49.
[10] V. Randle, O. Engler, Introduction to Texture Analysis: Macrotexture, Microtexture and Orientation & Mapping, CRC Press, 2009 (ISBN-10: 9056992244).
[11] V. Venegas, F. Caleyo, T. Baudin, J.H. Espina-Hernández, J.M. Hallen, On the role of crystallographic texture in mitigating hydrogen-induced cracking in pipeline steels, Corros. Sci. 53 (2011) 4204–4212.
[12] V. Venegas, F. Caleyo, T. Baudin, J.M. Hallen, R. Penelle, Role of microtexture in the interaction and coalescence of hydrogen-induced cracks, Corros. Sci. 51 (2009) 1140–1145.
[13] A. Ghosh, S. Kundu, D. Chakrabarti, Effect of crystallographic texture on the cleavage fracture mechanism and effective grain size of ferritic steel, Scr. Mater. 81 (2014) 8–11.
[14] J.I. Verdeja, J. Asensio, J.A. Pero-Sanz, Texture formability, lamellar tearing and HIC susceptibility of ferritic and low-carbon HSLA steels, Mater. Charact. 50 (2003) 81–86.
[15] M.A. Mohtadi-Bonab, M. Eskandari, J.A. Szpunar, Texture local misorientation, grain boundary and recrystallization fraction in pipeline steels related to hydrogen induced cracking, Mater. Sci. Eng. A 620 (2015) 97–106.
[16] M.A. Mohtadi-Bonab, M. Eskandari, K.M.M. Rahman, R. Ouellet, J.A. Szpunar, An extensive study of hydrogen-induced cracking susceptibility in an API X60 sour service pipeline steel, Int. J. Hydrog. Energy 41 (2016) 4185–4197.
[17] M.A. Mohtadi-Bonab, J.A. Szpunar, L. Collins, R. Stankievech, Evaluation of hydrogen induced cracking behavior of API X70 pipeline steel at different heat treatments, Int. J. Hydrog. Energy 39 (2014) 6076–6088.
[18] M.A. Arafin, J.A. Szpunar, A new understanding of intergranular stress corrosion cracking resistance of pipeline steel through grain boundary character and crystallographic texture studies, Corros. Sci. 51 (2009) 119–128.
[19] L.P.M. Santos, M. Béreš, I.N. Bastos, S.S.M. Tavares, H.F.G. Abreu, M.J. Gomes da Silva, Hydrogen embrittlement of ultra-high strength 300 grade maraging steel, Corros. Sci. 101 (2015) 12–18.
[20] M.A. Mohtadi-Bonab, J.A. Szpunar, S.S. Razavi-Tousi, A comparative study of hydrogen induced cracking behavior in API 5L X60 and X70 pipeline steels, Eng. Fail. Anal. 33 (2013) 163–175.
[21] N. Yazdipour, A.J. Haq, K. Muzaka, E.V. Pereloma, 2D modelling of the effect of grain size on hydrogen diffusion in X70 steel, Comput. Mater. Sci. 56 (2012) 49–57.
[22] E.O. Hall, The deformation and ageing of mild steel: III discussion of results, Proc. Phys. Soc. Lond. 64 (1951) 747–753.

[23] N.J. Petch, The cleavage strength of polycrystals, J. Iron Steel Inst. Lond. 173 (1953) 25–28.
[24] W. Zhou, Z.L. Wang, Scanning microscopy for nanotechnology, Genet. Anal. Technol. Appl. 12 (2007) 41–75.
[25] M. Koyama, E. Akiyama, T. Sawaguchi, K. Ogawa, I.V. Kireeva, Y.I. Chumlyakov, K. Tsuzaki, Hydrogen-assisted quasi-cleavage fracture in a single crystalline type 316 austenitic stainless steel, Corros. Sci. 75 (2013) 345–353.
[26] J. Weertman, Crack growth for the double slip plane and the modified DSP crack model-ii. fatigue crack growth with and without blunting, Acta Metall. 32 (4) (1984) 573–584.
[27] F.J. Humphreys, M. Hatherly, Recrystallization and related annealing phenomena, Australia (2004).
[28] R. Badji, T. Chauveau, B. Bacroix, Texture, misorientation and mechanical anisotropy in a deformed dual phase stainless steel weld joint, Mater. Sci. Eng. A 575 (2013) 94–103.
[29] H.K. Birnbaum, Mechanisms of hydrogen related fracture of metals, MRL (1989) 1–19.
[30] Specification for linepipe, API Specification 5L forty-third edition (2004).
[31] K. Fukui, A. Okamoto, Effect of graphite, cementite on mechanical properties of cold rolled, ISIJ Int. 76 (8) (1990) 1349–1355.
[32] D. Raabe, K. Lucke, G. Gottstein, Texture and microstructure of high purity tantalum, J. Phys. IV Colloque 3 (1993) 523–526.
[33] C.D. Singh, V. Ramaswamy, C. Suryanarayana, Texture evolution in a hot rolled austenitic stainless steel, Textures Microstruct. 13 (1991) 227–241.
[34] H. Hu, Texture of metals, Texture, Gordon and Breach Science Publishers Ltd. (1974) 233–258.
[35] I. Tamura, H. Sekine, T. Tanaka, C. Ouchi, Chapter 12—Further developments in thermomechanical processing. Thermomechanical Processing of High-Strength Low-Alloy Steels (1988) 226–236.
[36] N.L. Kareta, V.G. Mazur, Variation of ductile-brittle transition temperature with grain size, Strength Mater. 9 (1977) 214–217.
[37] J.H. Shen, Y.L. Li, Q. Wei, Statistic derivation of Taylor factors for polycrystalline metals with application to pure magnesium, Mater. Sci. Eng. A 582 (2013) 270–275.
[38] U.F. Kocks, H. Mecking, Physics and phenomenology of strain hardening: the FCC case, Prog. Mater. Sci. 48 (3) (2003) 171–273.
[39] M.D. Roach, S.I. Wright, J.E. Lemons, L.D. Zardiackas, An EBSD based comparison of the fatigue crack initiation mechanisms of nickel and nitrogen-stabilized cold-worked austenitic stainless steels, Mater. Sci. Eng. A 586 (2013) 382–391.
[40] K. Fukuya, H. Nishioka, K. Fujii, T. Miura, T. Torimaru, An EBSD examination of SUS316 stainless steel irradiated to 73 dpa and deformed at 593 K, J. Nucl. Mater. 417 (2011) 958–962.
[41] L. Novotný, Simulation of void growth in ductile steel under mechanical loading, Metalurgija 49 (2010) 416–419 (ISSN 0543-5846).
[42] M. Halama, D. Jerolitsch, J. Žilková, R. Dzedzina, P. Linhardt, Improvement of ENA-NOCS Technique Using Artificial Neural Networks Approach for the Detection of Corrosion Eurocorr 2010, MAKC Press, 2010, pp. 1–8.